Triaxial anisotropic magnetocaloric effect in the van der Waals antiferromagnet CrSBr

Yucheng Ye,[1,*] Liqiang Zeng,[1,*] Yuling Zhou,[1] Yuxuan Peng,[2] Mingzhu Xue,[3,4] Luis A. Montero-Cabrera,[5,6] Licong Peng,[7] Ziyang Gan,[8] Yue Chen,[1] Zhongchong Lin,[1,†] Jinbo Yang,[2] and Zhigao Huang[1,9,‡]

[1]*College of Physics and Energy, Fujian Normal University, Fujian Provincial Key Laboratory of Quantum Manipulation and New Energy Materials, Fuzhou 350117, People's Republic of China*

[2]*State Key Laboratory for Artificial Microstructure & Mesoscopic Physics, School of Physics, Peking University, Beijing 100871, People's Republic of China*

[3]*School of Physics and Astronomy, Beijing Normal University, Beijing 100875, People's Republic of China*

[4]*Key Laboratory of Multiscale Spin Physics (Ministry of Education), Beijing Normal University, Beijing 100875, People's Republic of China*

[5]*Laboratorio de Química Computacional y Teórica, Departamento de Química Física, Universidad de La Habana, 10400 Havana, Cuba*

[6]*Donostia International Physics Center (DIPC), Donostia − San Sebastián, Basque Country 20018, Spain*

[7]*School of Materials Science and Engineering, Peking University, Beijing 100871, People's Republic of China*

[8]*School of Physics and Electronics, Hunan Normal University, Changsha 410081, People's Republic of China*

[9]*Fujian Provincial Engineering Technical Research Centre of Solar-Energy Conversion and Stored Energy, Fuzhou 350117, People's Republic of China*

(Received 28 December 2025; revised 16 June 2026; accepted 13 August 2026; published 31 August 2026)

Magnetic anisotropy is a pivotal parameter that determines the magnetic ordering behavior and plays an important role in practical applications of magnetic materials. However, its influence on thermodynamic properties remains experimentally unexplored. As an air-stable, antiferromagnetic (AFM) van der Waals (vdW) semiconductor, CrSBr exhibits unique uniaxial in-plane magnetic anisotropy, making it an ideal platform to elucidate these unresolved relationships. Herein, high-quality CrSBr single crystals are synthesized via a modified two-step chemical vapor transport (CVT) method. A comprehensive analysis using modified Arrott plots, the Kouvel-Fisher method, the Widom scaling law, and critical isotherm analysis confirms a possible direct crossover from the tricritical mean-field behavior to the 3D Ising behavior, suggesting non-negligible interlayer coupling in bulk CrSBr. Supported by first-principles calculations and molecular field approximations, a pronounced triaxial magnetic anisotropy is quantified, with relative anisotropy energy satisfying $K(b \rightarrow c) > K(b \rightarrow a)$. Notably, strong anisotropy energy overcomes the interlayer exchange coupling ($K > JS^2$), driving a field-induced first-order spin-flip transition along the easy b axis. The maximum magnetic entropy change ($-\Delta S_{\mathrm{M}}^{\mathrm{max}}$) is 5.21, 5.09 and 4.74 J/(kg K) for $H \parallel b$, $H \parallel a$, and $H \parallel c$, respectively. Pronounced in-plane uniaxial magnetic anisotropy guarantees an anisotropic magnetocaloric effect, as evidenced by a negative linear correlation between K and rotating magnetic entropy change $-\Delta S_{\mathrm{M}}^{\mathrm{R}}$. These findings contribute to understanding of magnetism and associated thermodynamic properties in triaxially magnetically anisotropic CrSBr, thereby facilitating the tuning of magnetic anisotropy and exotic spin states in two-dimensional magnets.

DOI: 10.1103/g97j-4cz4

I. INTRODUCTION

Since the discovery of chromium-based van der Waals (vdW) layered magnets CrI_3 and $CrGeTe_3$ [1,2], magnetic anisotropy has been known as a key parameter to maintain magnetic ordering in the two-dimensional (2D) limit, breaking through the Mermin-Wagner theorem [3,4]. Owing to tunable magnetic anisotropy and controllable magnetic stacking configurations, chromium-based 2D magnets have potential applications in constructing atomically thin spintronic devices and nonvolatile magnetic storage devices [5–7]. Nevertheless, their sub-liquid-nitrogen ordering temperature and ambient sensitivity pose significant barriers to integrating these materials into practical devices—limitations shared by most studied 2D magnetic systems.

CrSBr, a ternary vdW antiferromagnetic (AFM) semiconductor, has emerged as a highly attractive candidate to overcome the aforementioned shortcomings. CrSBr demonstrates remarkable air stability under normal environmental conditions and a high bulk Néel temperature (T_{N}) of 132 K, which increases with decreasing layer number [8–10]. In particular, its A-type AFM ordering, characterized by extraordinary in-plane magnetic anisotropy, offers substantial opportunities for manipulating magnetic device functionalities, including magnetoelectric, magneto-optical, and spintronic devices [11]. Shao *et al.* [12] reported the discovery of a magnetic surface exciton in CrSBr, which originates from AFM spin correlations. Yang *et al.* [13] achieved surface plasmon polaritons with highly anisotropic propagation

*These authors contributed equally to this work.
†Contact author: zclin@fjnu.edu.cn
‡Contact author: zghuang@fjnu.edu.cn

characteristics by engineering a graphene/CrSBr heterostructure. Recently, by twisting two bilayers of CrSBr, a fully AFM tunnel junction has been constructed with a more than 700% nonvolatile tunneling magnetoresistance ratio achieved in zero magnetic fields [14]. In the development of device applications, the fundamental magnetocaloric properties remain a critical consideration. A recent theoretical prediction for the Cr-based vdW magnet CrI_3 found that magnetocrystalline anisotropy energy (MAE) could contribute to the anisotropic magnetocaloric response by influencing magnetization dynamics [15]. However, direct experimental evidence is still rare in 2D magnets. CrSBr is theoretically and experimentally predicted to exhibit well triaxial magnetic anisotropy [16,17], making it an ideal platform for understanding magnetic anisotropy-related magnetocaloric effect in 2D magnets. Recent studies revealed that temperature-dependent multiphase transitions in CrSBr enhance entropy change [18], and spin entropy in CrSBr flakes significantly boosts the Seebeck coefficient and then can improve thermoelectric conversion efficiency [19]. However, the relationship between magnetic entropy and magnetic anisotropy has yet to be elucidated. Understanding anisotropic thermodynamic effects can help elucidate the connection between magnetic anisotropy and long-range magnetic order in two-dimensional Heisenberg systems with isotropic exchange. Besides, recently observed peculiar magnetic behaviors in CrSBr deserve attention. The second harmonic generation confirms that the T_N of CrSBr increases with decreasing layer number, suggesting the presence of a hidden intermediate magnetic phase above T_N [9]. Below T_N, an extra ferromagnetic (FM) phase can be observed with a sharp increase of magnetization onsetting at ∼35 K, which is attributed to the FM ordering of magnetic defects, the slowing down of magnetic fluctuations and spin freezing, or the ionization of the Br/S vacancies [18,20–22]. Multiple phase transitions suggest complex interatomic interactions in such an orthorhombic structure with anisotropic crystal axes ($a \neq b \neq c$). Consequently, it is essential to reveal the fundamental magnetic properties of highly crystalline bulk CrSBr—particularly the temperature-dependent spin ordering with critical behaviors and triaxial magnetic anisotropy with related magnetocaloric effect.

In this work, high-quality CrSBr single crystals were synthesized by a custom-built chemical vapor transport (CVT) method to systematically investigate the aforementioned unresolved questions through comprehensive structural and magnetic characterizations. The combination of the modified Arrott plot, the Kouvel-Fisher plot, the Widom scaling law, and critical isotherm analysis around second-order magnetic transition near 135 K indicates a crossover-like critical behavior between tricritical mean-field and 3D Ising limit [$\beta = 0.265(8)$, $\gamma = 1.297(1)$, and $\delta = 5.71(9)$]. Further quantitative calculation by the molecular field approximation reveals triaxial magnetic anisotropy and first-order spin-flip transition in CrSBr. Macroscopically, this triaxial anisotropy is explicitly reflected in the thermodynamic response, yielding an anisotropic magnetocaloric effect with maximum magnetic entropy changes ($-\Delta S_M^{max}$) of 5.21, 5.09 and 4.74 J/(kg K) along the *b*, *a*, and *c* axes at 5 T, respectively. Consequently, the rotating magnetic entropy $-\Delta S_M^R$ exhibits a strong crystallographic orientation dependence with ΔS_M^R $(b \rightarrow c) > -\Delta S_M^R$ $(b \rightarrow a)$. Our findings provide fundamental insights into magnetic transition mechanisms from the perspectives of magnetic exchange and anisotropy energy, while establishing a comprehensive analysis of the magnetic anisotropy-driven magnetocaloric effect, where the temperature and magnetic field dependence of magnetic anisotropy is a key factor that affects the thermodynamic properties.

II. EXPERIMENTAL DETAILS

The single crystals of CrSBr were prepared using a modified CVT method with a two-step transport process [23]. I. $2Cr + 3Br_2 \rightarrow 2CrBr_3$: High-quality chromium tribromide ($CrBr_3$) was synthesized via CVT using mixed chromium (99.996%, Alfa Aesar) and $TeBr_4$ (99.999%, Alfa Aesar) powders with a stoichiometric ratio of 1 : 0.75. The mixture was sealed in an evacuated quartz tube and placed in a two-zone tubular furnace. The source end was kept at 973 K, and the sink was kept at 853 K for 7 days during the growth. After CVT growth, the black crystals of $CrBr_3$ were formed on the cold side of the tube [24]. II. $2Cr + 3S + CrBr_3 \rightarrow 3CrSBr$: chromium (99.996%, Alfa Aesar), sulfur pieces (99.9995%, Alfa Aesar), and $CrBr_3$ were sealed within a quartz tube and positioned in a dual-zone tube furnace. The source zone and growth zone were heated to 1123 and 1223 K, respectively, within 24 hours and maintained at these temperatures for 48 hours. Subsequently, the temperature of the two zones was reversed: the source zone was heated to 1223 K while the growth zone was cooled to 1123 K over 12 hours. The temperatures were then maintained for 48 hours, after which both ends were cooled to room temperature naturally. The strip-like crystals were purified by immersion in a 1 mg/mL aqueous $CrCl_2$ solution for 1 hour at room temperature to remove unreacted precursors. The solution was decanted, followed by sequential rinsing with deionized water and acetone to eliminate residual sulfur and organic impurities to ensure the formation of stoichiometrically precise, defect-minimized CrSBr crystals.

The crystal structure of the sample was determined by x-ray diffraction (XRD) using a Rigaku Mini-Flex II diffractometer with Cu $K\alpha$ radiation ($\lambda = 1.5406$ Å). The structural refinement was performed using the FULLPROF software based on the *Le Bail* method with the peak profile of Pseudo-Voigt functions [25,26]. To further elucidate the complete crystallographic structure and in-plane order, single-crystal x-ray diffraction was performed using a Rigaku XtaLAB Synergy single-crystal diffractometer. Data collection, integration, absorption correction, and structural refinement were carried out using Olex2. The morphology was examined by scanning electron microscopy (SEM) (JSM-7800F, JEOL), which is equipped with an energy-dispersive x-ray spectrometer (EDS) to obtain a quantitative analysis of chemical composition. X-ray photoelectron spectroscopy (XPS, ESCALAB Xi+) was applied to analyze the information about the surface chemical state of the single crystal. Magnetic properties and heat capacity of CrSBr were investigated using a Quantum Design Physical Properties Measurement System (PPMS-9T) with a vibrating sample magnetometer (VSM). A single crystal with 2.50 mm × 1.44 mm × 0.16 mm was used for magnetic measurements, and the oscillatory demagnetization protocols were rigorously applied prior to each experimen-

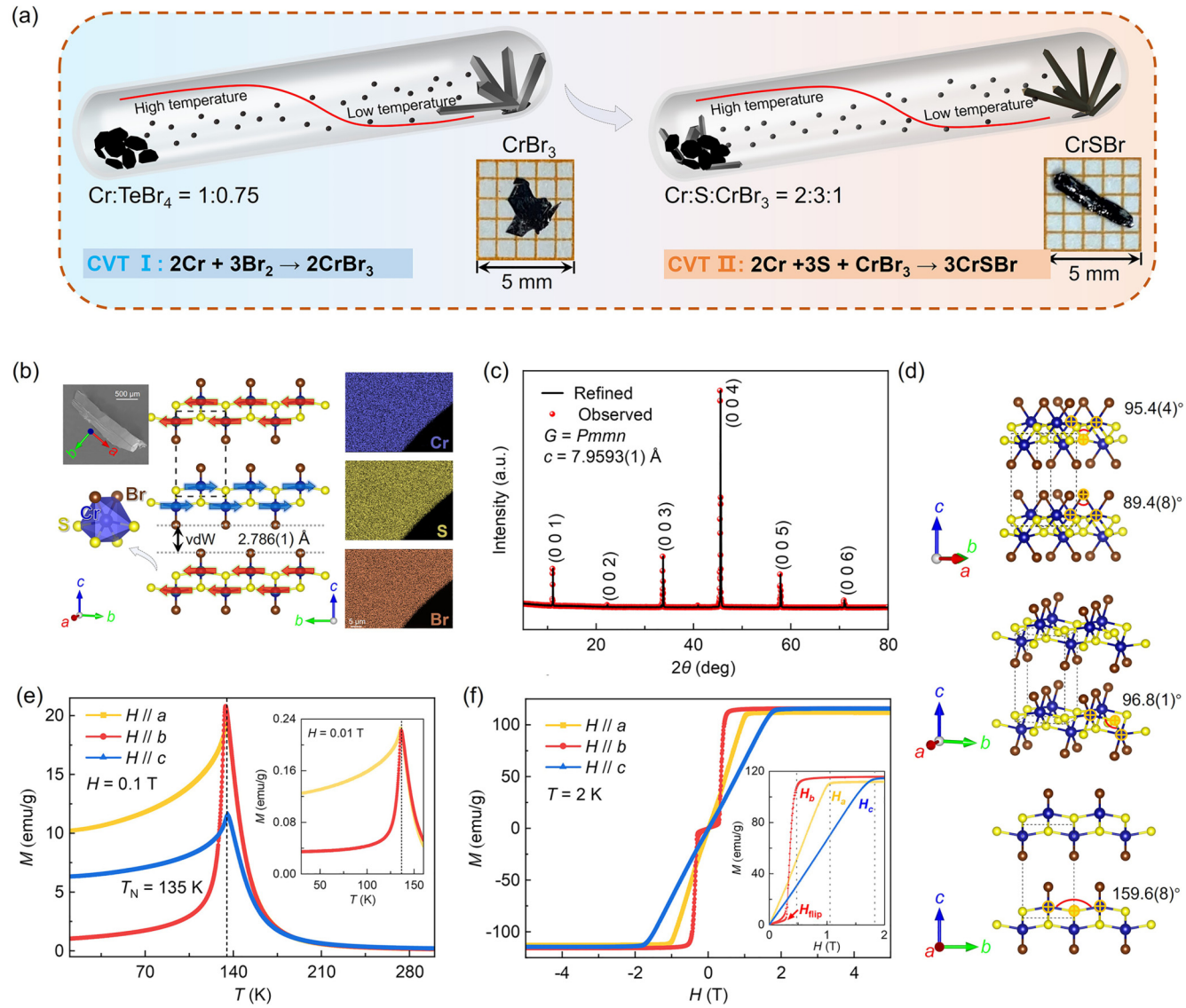

FIG. 1. (a) A schematic diagram of the experimental procedure for growing CrSBr single crystals via a two-step method. (b) Photograph of bulk single-crystal CrSBr on a grid paper, the A-type magnetic structure of CrSBr from side view, and the EDS mappings of the Cr, S, and Br in the CrSBr flake. (c) The refined XRD pattern of single-crystal CrSBr at room temperature. (d) The three bond angles for intralayer superexchange paths in CrSBr structure. (e) Temperature-dependent zero-field-cooled (ZFC) magnetization under an applied field of 0.1 T parallel to crystallographic a, b, and c axes. The inset shows ZFC M-T curve under an applied field of 0.01 T parallel to a and b axes. (f) At 2 K, field-dependent magnetization with field parallel to a, b, and c axes, respectively. The inset is the enlarged part of (f).

tal run to eliminate residual magnetic field artifacts. The demagnetization-corrected magnetization curves were subsequently derived using the relation $H = \mu_0 H - 4\pi NM$, where N represents the geometry-dependent demagnetization factor. For $H \parallel c$, N is 0.822, N is 0.114 for $H \parallel b$, and N is 0.064 for $H \parallel a$, consistent with the platelet-like morphology of the CrSBr crystal. The calculation of N is provided in Note S1 of Supplemental Material (SM) [Eq. S(1)] [27]. The characteristic fields used in the M-H analysis were determined from the demagnetization-corrected magnetization curves. The relevant saturation fields, including the spin-flip field H_{flip} and the saturation fields H_s^b for $H \parallel b$, H_s^a for $H \parallel a$, and H_s^c for $H \parallel c$. Specifically, using the magnetization curve along for $H \parallel b$ as an example in Fig. 1(f), H_{flip} is determined by the maximum of the first derivative curve dM/dH, while the saturation field H_s^b is identified as the point where dM/dH returns to the near-zero level following the spin-flip transition.

First-principles calculations based on density functional theory (DFT) were performed using the Vienna *Ab initio* Simulation Package (VASP) [46,47], applying the exchange-correlation description of GGA [48]. An on-site Hubbard term $U = 4$ eV and Hund's exchange coupling $J_H = 0.9$ eV were used for Cr-d orbitals. Brillouin zone integrations were performed using a Γ-centered Monkhorst-Pack k-point grid of $9 \times 7 \times 4$. Spin-orbit coupling (SOC) was self-consistently included in the calculations of magnetic anisotropy energy (MAE). The plane-wave cutoff energy was taken as 500 eV, and the energy and force convergence criteria for structural relaxation were set to 10^{-6} eV and 0.01 eV/Å.

III. RESULTS AND DISCUSSION

A. Structure and intrinsic magnetism

CrSBr single crystals were synthesized via a two-step method, as illustrated in Fig. 1(a). Initially, $CrBr_3$ single crystals were grown [24], which subsequently served as a precursor for the reaction with additional Cr and S to form the final CrSBr crystals. Detailed synthesis and growth procedures are provided in the Experimental details. As shown in Fig. 1(a), CrSBr single crystals can be grown to a striplike millimeter size ($\sim$5.0 mm $\times$ 1.5 mm $\times$ 0.5 mm). The long side of the crystal coincides with the crystallographic a axis, and the short side is along the crystallographic b axis, manifesting the in-plane lattice structural anisotropy as earlier reported [23]. The EDS mappings revealed the homogeneous elemental distribution of Cr, S, and Br without detectable impurities, which is further supported by multi-area statistical measurements (Note S2 in SM [27]). The corresponding EDS spectrum demonstrated strong signals of Cr, S, and Br, which is consistent with the expected stoichiometric ratio of CrSBr Fig. 1(b)]. XPS analysis of the CrSBr crystal identified Cr, S, and Br, with an atomic ratio close to the EDS results, as shown in Fig. S2 and Note S3 in SM [27]. Deconvolution of the high-resolution spectra yielded the following peaks: Cr $2p_{3/2}$ and $2p_{1/2}$ at 575.7 and 585.1 eV, S $2p_{3/2}$ and $2p_{1/2}$ at 161.9 and 163.1 eV, and Br $3d_{5/2}$ and $3d_{3/2}$ at 68.8 and 69.7 eV. The observed binding energies agree with reported values for Cr^{3+}, S^{2-}, and Br^{-}, validating the expected S–Cr–Br bonding and the high quality of the synthesized material [49]. The XRD pattern contains only $(00l)$ peaks and has a narrow full width at half maximum ($< 0.02^{\circ}$), indicating high-quality single crystallinity of the as-grown bulk crystal [Fig. 1(c)]. The *Le Bail* refinement of the XRD pattern indicates that the layered structure of CrSBr belongs to the orthorhombic space group *Pmmn* (No. 59) with the vdW gap of 2.786(1) Å, as illustrated in Fig. 1(b). This structure was further confirmed by single-crystal x-ray diffraction, which precisely determined the lattice parameters to be $a = 3.5141(8)$ Å, $b = 4.7499(12)$ Å, and $c = 7.9428(17)$ Å (Fig. S3), consistent with previous reports [9,50]. Within this structure, as illustrated in Fig. 1(b), each layer consists of two buckled CrS planes sandwiched between Br sheets. The local coordination environment of each Cr ion is a distorted $[CrS_4Br_2]$ octahedron with local C_{2v} symmetry, indicating pronounced structural anisotropy along all three crystallographic directions. Temperature- and field-dependent magnetic measurements were further conducted to investigate the magnetic properties of CrSBr. Figure 1(e) exhibits zero-field-cooled (ZFC) magnetization characteristics of CrSBr for an applied field of 0.1 T parallel to the a, b, and $c$axes, respectively. The T_N, manifested as a peak in the ZFC curve, can be observed at around 135 K. The smaller magnetization for $H \parallel b$ below the T_N indicates the bulk easy-magnetization axis along the b direction. According to the Curie-Weiss law, the high-temperature magnetization (above 150 K) can be fitted, and the Weiss temperature T_θ can be obtained as 175.8, 157.7, and 155.3 K for $H \parallel a$, b, and c from the least-squares analysis (Fig. S4, SM [27]), respectively. The fitted T_θ values are positive and close to T_N, confirming the local FM coupling between moments. This is consistent with the A-type AFM structure as shown in Fig. 1(b), where neighboring Cr moments form intralayer FM interactions.

As we know, the direct exchange arising from the electron hopping between the nearest neighbor Cr sites, formed from the $3d$ orbitals, is AFM in nature restricted by the Pauli exclusion principle [51]. However, as the nearest Cr-Cr distance in a monolayer of CrSBr is 3.54 Å, much larger than 2.52 Å for Cr metal in the Bethe-Slater curve, the direct interaction is weaker than the superexchange interaction mediated by the S/Br anions between Cr ions in CrSBr. According to the Goodenough-Kanamori-Anderson rules [52], the superexchange interaction between two Cr atoms is ferromagnetic for a 90°Cr-S/Br-Cr angle, and is AFM for a 180°Cr-S/Br-Cr angle. As depicted in Fig. 1(d), the chemical bonding along the basal directions involves Cr-S/Br-Cr paths along the a axis with a cation-anion-cation angle of 95.4(4)°/89.4(8)°, and Cr-S-Cr paths along the c axis with a cation-anion-cation angle of 96.8(1)°, while Cr-S-Cr paths along the b axis exhibit an angle of 159.6(8)°. It is not surprising that FM interactions occur along the a and c axes in the monolayer. This suggests competing AFM and FM contributions along the b axis. Conversely, the interlayer coupling across the vdW gap along the macroscopic c axis is dominated by weak supersuperexchange, which stabilizes the AFM coupling to form the A-type AFM. Some studies show multiple phase transitions in CrSBr, notably including an intermediate FM ordered phase near 145 K, and a FM-like phase near 35 K. Some studies found a high defect concentration in heavily n-type doped crystals grown via a one-step CVT synthesis using Cr_2S_2 and Br_2 as precursors, which contributes to the anomalous increase in magnetic susceptibility observed at 35 K. Nevertheless, following a two-step CVT growth protocol similar to that of A. Scheie *et al.* [23], no abnormal kinks are observed in our M-T curves with applied fields of 0.1 and 0.01 T [Fig. 1(e) and its inset], indicating no detectable signs of magnetic defects or secondary magnetic ordering phenomena in our high-crystallinity CrSBr crystal.

B. Triaxial magnetic anisotropy of CrSBr

The metamagnetic transition and magnetic anisotropy are further analyzed by field-dependent magnetization curves with the magnetic fields parallel to different crystallographic axes at 2 K, as shown in Fig. 1(f). The M-H curves at $T = 2$ K show a typical AFM feature with negligible magnetic susceptibility in low fields. Notably, for $H \parallel b$, by increasing H to a critical field $H_{\text{flip}} = 0.35(8)$ T, the magnetization exhibits a sharp and nonlinear increase and then becomes saturated rapidly above $H_s^b = 0.58(4)$ T, indicating a field-induced metamagnetic transition. For $H \parallel a$ and $H \parallel c$, the metamagnetic transition is not observed. Instead, there is linear M growth and larger high-field saturation behavior with H_s^a of 1.09(0) T and H_s^c of 1.84(6) T, respectively. Such an anisotropic field response is consistent with previous magnetization studies on high-quality CrSBr crystals [53]. This arises from the reconstruction of the spin-moment arrangement, which gradually transitions from the bulk easy axis (b axis) to the ac plane, inducing canted antiferromagnetism. In the octahedral crystal field of $[CrS_4Br_2]$, the $3d$ orbitals of Cr undergo splitting. This

results in a lower-energy triplet state t_{2g} (d_{xy}, d_{yz}, and d_{xz}) and a higher-energy doublet state e_g ($d_{x^2-y^2}$ and d_{z^2}). In accordance with Hund's rule, the remaining three electrons of Cr^{3+} ($3d^3$) fill the t_{2g} state. The absence of orbital degeneracy results in an orbital singlet with a quenched orbital moment [54,55]. As shown in Fig. 1(f), the saturated magnetization gives a magnetic moment of $m_s \approx 3.4\,\mu_B$/Cr, confirming a largely quenched orbital moment. In the single axis case, the Hamiltonian of the collinear AFM system CrSBr is mainly determined by AFM exchange interaction, magnetocrystalline anisotropic energy, and Zeeman energy [56];

$$\mathcal{H} = J\sum \vec{S}_i \cdot \vec{S}_j - K\left(\sum S_{iy}^2 + \sum S_{jy}^2\right) - g\mu_B H_0\left(\sum S_{iy} + \sum S_{jy}\right), \quad (1)$$

where S_i and S_j are the spins at sites i and j of the sublattice. S can be obtained by $m_s = g\mu_B\sqrt{S(S+1)}$, where $g = 2$. J is the exchange constant of the interaction between spins S_i and S_j. The K term represents the uniaxial anisotropy of a single axis and the last term is the usual Zeeman term (μ_B is the Bohr magneton, and H_0 is the applied static magnetic field along the y direction). With the field applied parallel to the magnetic easy axis, the molecular field approximation based on a semi-classical model gives critical fields as [57]

$$H_S = 2H_{AF} - H_A, \quad (2)$$

where $H_{AF} = JS^2/g\mu_B S$ is AFM exchange field, and $H_A = 2K/g\mu_B S$ is the anisotropy field based on the two-spin macrospin model. The H_A can be further subdivided into $H_A^{ba} = H_S^b - H_S^a$ and $H_A^{bc} = H_S^b - H_S^c$, representing the effective anisotropy fields between the b and a axes and between the b and c axes, respectively [58]. Thus we can calculate $K = 0.047(1)$ meV and $JS^2 = 0.112(7)$ meV for the b axis versus a axis, and $K = 0.124(6)$ meV and $JS^2 = 0.078(6)$ meV for the b versus c axis. This indicates that bulk CrSBr has the easy magnetization b, hard c, and intermediate a axes.

To further corroborate the experimentally determined triaxial anisotropy, first-principles calculations based on three spin-quantization directions for the same A-type AFM configuration were performed, with the spin quantization axis constrained along the crystallographic b, a, and c directions. Detailed computational methods and magnetic configurations are provided in Note S6 of SM [27]. As shown in Table S4, the calculated relative MAE values (defined as $\Delta E_i = E_i - E_b$) are 0, 82, and 89 μeV/Cr for the b, a, and c axes, respectively. This confirms the b axis as the easy magnetization axis, the c axis as the hard axis, and the a axis as the intermediate axis, consistent with our molecular-field analysis and previous studies [17]. As aforementioned, due to quenched orbital moments, the lowest order nonzero contribution of magnetic anisotropy energy arises from quantum fluctuations of the orbital moments [54], which is quadratic and vanishes in a perfect octahedral environment. However, the local distortion of the CrS_4Br_2 octahedra yields magnetic anisotropy due to uniaxial anisotropy derived from spin-orbit coupling and shape anisotropy attributed to the magnetic dipole-dipole interaction of Br ions, as reported by early first-principles calculations and Monte Carlo simulations [17,59]. Meanwhile, the larger anisotropy energy than that of exchange coupling between the easy and hard axes is conventionally interpreted as a hallmark of the spin-flip transition in AFM systems like $(Fe, Co)_3GaTe_2$, which is different from the strong exchange interactions of spin-flop in $CrPS_4$ and $MnBi_2Te_4$ [60,61].

C. Arrott plots and phase transition behavior

Figures 2(a)–2(c) present the isothermal magnetization curves of CrSBr under magnetic fields up to 5 T from 84 to 204 K for $H \parallel a$, $H \parallel b$ and $H \parallel c$, respectively. Below T_N of 135 K, the magnetizations at all crystallographic axes increase dramatically with applied field, until the curves plateau near the saturation field H_S. Noticeably, the spin-flip transition for $H \parallel b$ can be observed, and its H_{flip} dwindles and vanishes at 135 K as the temperature increases, which is related to the temperature scaling of anisotropy energy. Meanwhile, the magnetization along all crystallographic axes gradually exhibits linear paramagnetic behavior as the temperature increases above T_N. To precisely determine the magnetic ordering near the transition temperature, we performed the critical-exponent analysis within the Widom scaling framework including the modified Arrott plot, the Kouvel-Fisher method, the Widom scaling law, and critical isotherm analysis (Note S7 in SM [27]). The Arrott plots of M^2 versus H/M are presented in Figs. 2(d)–2(f). As previously mentioned, the only AFM exchange coupling in A-type AFM CrSBr is interlayer coupling mediated by the vdW gap, which usually makes it small, especially compared to those with intralayer exchange coupling. Therefore the saturated fields of CrSBr are small (less than 2 T), and the M^2 versus H/M curves near the transition temperature should be parallel straight lines in the high-field region with the same slope of $S(T) = dM^{1/\beta}/d(H/M)^{1/\gamma}$. In Figs. 2(d)–2(f), the curves are nonlinear in the high-field region, suggesting that the mean-field theory is inadequate for accurately characterizing the critical behavior of CrSBr. Thus the critical behavior is systematically investigated by means of the modified Arrott plot (MAP) for $H \parallel c$ based on five canonical theoretical models, including 2D Ising ($\beta = 0.125$, $\gamma = 1.75$), 3D Ising ($\beta = 0.325$, $\gamma = 1.24$), 3D XY ($\beta = 0.345$, $\gamma = 1.316$), 3D Heisenberg ($\beta = 0.365$, $\gamma = 1.386$), and tricritical mean-field ($\beta = 0.25$, $\gamma = 1$), as shown in Figs. S7(c)–S7(g) in SM [27]. The derivation of the MAP is provided in Eq. S(3). The normalized slopes $NS = S(T)/S(T_N)$ are summarized and compared to the ideal value of 1 to determine the most appropriate model, as depicted in Fig. S7(h). The 2D Ising and tricritical mean-field models agree most closely with the experimental data, exhibiting the least deviation.

The tricritical mean-field exponents ($\beta = 0.25$, $\gamma = 1$) were selected as initial parameters for further iterative analysis. A new modified Arrott plot can be drawn based on the obtained β and γ values. This process is iterated until β and γ are stable and the detailed iterative method can be seen in Eqs. S(4)–S(6). Figure 2(g) shows the final converged critical exponents $\beta = 0.265(8)$ with $T_t = 137.216(1)$ K, and $\gamma = 1.297(1)$ with magnetic transition temperature $(T_t) = 137.277(6)$ K. Besides, the critical exponent can also be evaluated by the KF method [Eqs. S(8) and S(9)], the linear fitting gives $\beta = 0.273(2)$ with $T_t = 137.350(2)$ K and $\gamma = 1.263(1)$ with $T_t = 137.314(7)$ K [Fig. 2(h)]. These val-

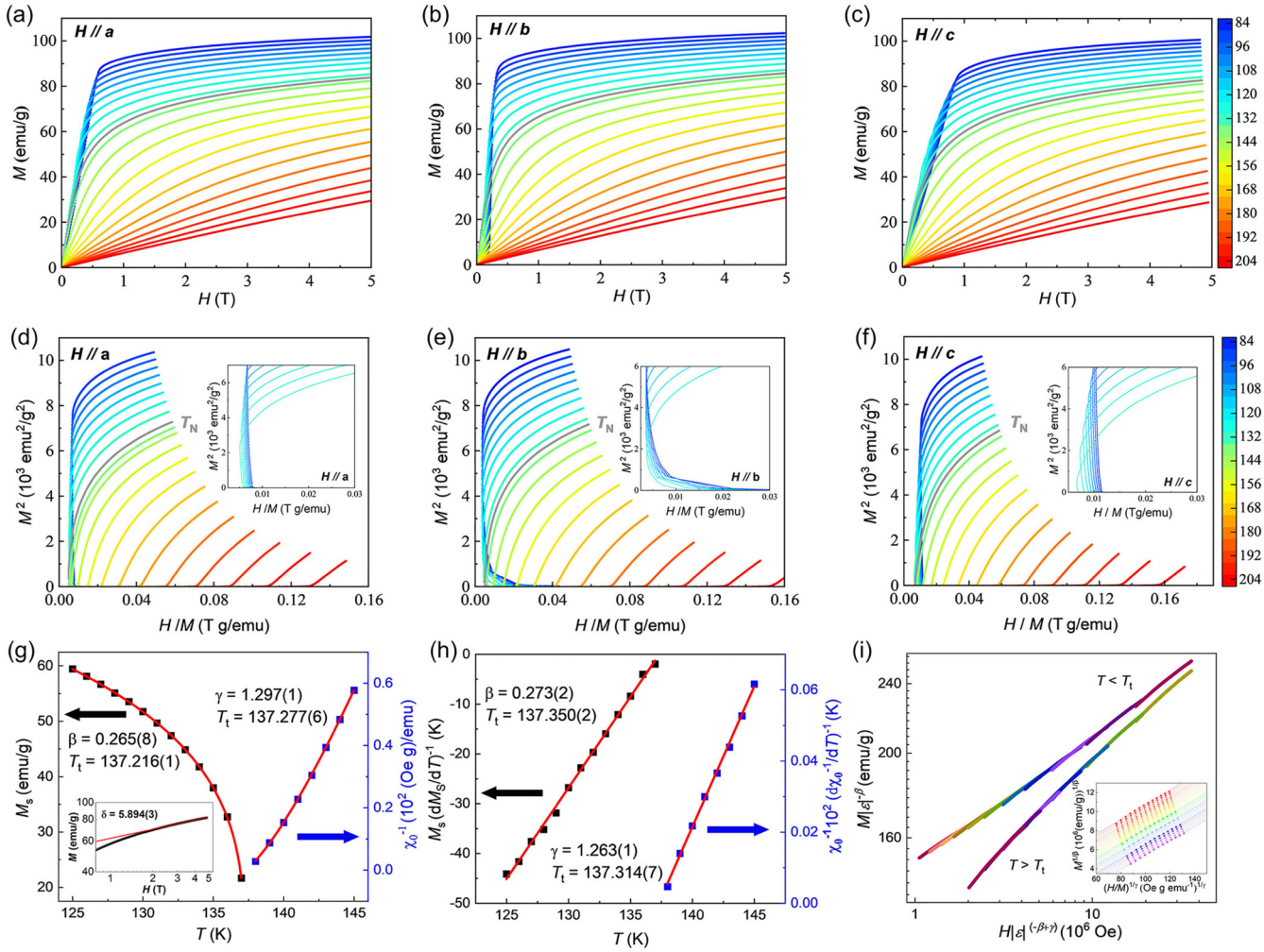

FIG. 2. The isothermal magnetization curves of CrSBr from 84 to 204 K with (a) $H \parallel a$, (b) $H \parallel b$, and (c) $H \parallel c$. (d), (e), and (f) are Arrott plots with $H \parallel a$, $H \parallel b$, and $H \parallel c$, respectively. The data are taken at $\Delta T = 6$ K intervals from 84 to 204 K. (g) The temperature dependence of the spontaneous magnetization M_S and the inverse initial magnetization χ_0^{-1} and their corresponding red fitting curves. The inset is the field-dependent magnetization scale plot on a log-log scale with the red fitting curve at 137 K. (h) Kouvel-Fisher (KF) plots of $M_S(T)(\frac{dM_S(T)}{dT})^{-1}$ and $\frac{\chi_0^{-1}}{d\chi_0^{-1}(T)/dT}$ with the red fitting curves. (i) The log-log plot of the reduced magnetization ($m = M|\varepsilon|^{-\beta}$) vs the reduced field ($h = H|\varepsilon|^{-(\beta+\gamma)}$) above and below Tt. The inset is the modified Arrott plots of isotherms in the temperature range from 125 to 145 K, where $\beta = 0.265$ and $\gamma = 1.297$ for the applied field $H \parallel c$.

ues are in close agreement with those obtained from the modified Arrott plot, indicating that the extracted constants are intrinsic. The critical isotherm at T_t, shown in the inset of Fig. 2(g), gives $\delta = 5.719(5)$, which is close to those estimated from the Widom relation $\delta = 1 + \gamma/\beta$, using the MAP and KF exponents, which gives $\delta = 5.89(15)$ and $\delta = 5.626(34)$, respectively. In addition to the Widom relation, representative scaling relations were examined in Note S7 of SM [27], such as the α values derived from the Rushbrooke and Griffiths relations. The obtained exponents are summarized in Table I together with representative theoretical values. A detailed comparison reveals that the extracted β and α values reside exactly between the tricritical mean-field and 3D Ising limits. Meanwhile, γ is slightly larger than the 3D Ising value, and δ slightly exceeds the tricritical mean-field value. Collectively, this specific distribution of exponents signifies a crossover-like 3D critical behavior, suggesting the complex mixed-exchange interactions within the system.

As a further consistency check within the Widom scaling framework, the rescaled magnetization data are plotted as $M|\varepsilon|^{-\beta}$ versus $H|\varepsilon|^{-(\beta+\gamma)}$, where $\varepsilon = (T - T_t)/T_t$. As shown in Fig. 2(i), the data fall onto two separate branches above and below T_t, respectively. This scaling collapse supports the internal consistency of the extracted exponents. The modified Arrott plots for the CrSBr single crystal reveal that the isotherms are parallel and linear, indicating marked linear behavior [the inset of Fig. 2(i)]. Moreover, according to Banerjee's criterion [62], the order of a magnetic transition can be preliminarily assessed via the slope of Arrott plots, where positive slopes correspond to second-order magnetic transitions and negative slopes correspond to first-order magnetic transitions. Clearly, in high-field regions for $H \parallel a$, $H \parallel b$, and $H \parallel c$, the concave downward curvature with positive

TABLE I. Comparison of the critical exponents α, β, γ, and δ of CrSBr with different theoretical models.

Composition	Reference	Method	α	β	γ	δ
CrSBr	This work	Modified Arrott plot	0.173	0.265(8)	1.297(1)	5.89(15)
CrSBr	This work	Kouvel–Fisher plot	0.191	0.273(2)	1.263(1)	5.626(34)
CrSBr	This work	Critical isotherm	—	—	—	5.719(5)
Mean-field	[63]	Theory	0	0.5	1.0	3.0
2D Ising	[63]	Theory	0	0.125	1.75	15.0
3D Ising	[63]	Theory	0.110	0.325	1.24	4.82
3D XY	[64]	Theory	−0.007	0.345	1.316	4.81
3D Heisenberg	[64]	Theory	−0.115	0.365	1.386	4.80
Tricritical mean-field	[64]	Theory	0.5	0.25	1.0	5.0

slopes around T_N suggests a second-order phase transition in CrSBr. By comparison, the low-field paramagnetic transition and field-induced transition are first-order transitions, as evidenced by the negative slopes of Arrott plots. Notably, a detailed examination of the magnified Arrott plots in Figs. 2(d)–2(f) reveals a marked distinction in the *b*-axis behavior compared to the *a* and *c* axes at low temperatures. The *b*- axis plot exhibits a significantly steeper curvature in its slope, a feature directly attributed to the spin-flip transition. This pronounced deviation underscores the critical role of spin-flip dynamics in driving the abrupt magnetic reconfiguration along the *b* axis, further corroborating the discontinuous character of the transition.

D. Anisotropic magnetocaloric effect

The magnetocaloric effect, an intrinsic property of magnetic materials, arises from changes in the magnetic entropy of the system due to the coupling between magnetic moments and an external magnetic field [65]. The isothermal magnetic entropy change (ΔS_M), recognized as a critical parameter for quantifying the magnetocaloric effect, is defined as [66]

$$\Delta S_M(T,H) = \int_0^H \left(\frac{\partial S}{\partial H}\right)_T dH = \int_0^H \left(\frac{\partial M}{\partial T}\right)_H dH, \quad (3)$$

where $(\frac{\partial S}{\partial H})_{T,P} = (\frac{\partial M}{\partial T})_{H,P}$ can be derived from isothermal magnetization curves using the Maxwell relations. When the magnetization measurement is performed within a narrow interval of temperature and magnetic field, Eq. (3) can be rewritten as [67]

$$\left|\Delta S_M\left(\frac{T_i + T_{i+1}}{2}, H\right)\right| = \sum_i \left[\frac{(M_i - M_{i+1})_{H_i}}{T_{i+1} - T_i}\right]\Delta H_i. \quad (4)$$

Figures 3(a)–3(c) illustrate the temperature dependence of $-\Delta S_M$ under varying magnetic field changes for $H \parallel a$, $H \parallel b$, and $H \parallel c$, respectively. Obviously, in FM systems maintained at a specific temperature, an applied magnetic field typically induces alignment of magnetic moments, thereby reducing the system's entropy and yielding a negative magnetic entropy change ($-\Delta S_M > 0$). In contrast, AFM materials exhibit unconventional magnetocaloric behavior. At low magnetic fields, the initially antiparallel spin configuration undergoes partial disruption, amplifying magnetic disorder and paradoxically elevating the magnetic entropy ($-\Delta S_M < 0$). This entropy enhancement emerges from the competition between field-induced spin reorientation and inherent AFM ordering. As the external field surpasses the critical threshold, the moments gradually transition into field-aligned configurations, restoring conventional entropy reduction ($-\Delta S_M > 0$) through progressive magnetic ordering.

For $H \parallel a$, b, and c, the overall trends of the curves are nearly identical. Observations indicate that for CrSBr below T_N, $-\Delta S_M$ is negative as the magnetic field changes from 0 to 0.5 T, signifying the presence of AFM ordering. As the field and temperature increase, the magnetic entropy change of CrSBr becomes negative ($-\Delta S_M > 0$) due to field-induced AFM-to-FM phase transition. All $-\Delta S_M$ curves exhibit pronounced peaks near T_N, with the peak profiles broadening asymmetrically toward both lower- and higher-temperature sides as the magnetic field strength increases. At $H = 5\,T$, the maximum magnetic entropy change $-\Delta S_M^{max}$ reaches 5.21 J/(kg K) when the magnetic field is parallel to the easily magnetized *b* axis. As summarized in Fig. 4(f), this value indicates that CrSBr exhibits a relatively considerable magnetocaloric response among reported vdW magnetic materials. At $H = 5$ T, the $-\Delta S_M^{max}$ reaches 5.21 J/(kg K) when the magnetic field is parallel to the easily magnetized *b* axis, which is competitive among representative vdW magnetic materials, as shown in Fig. 4(f), such as $Fe_{3-x}GeTe_2$ [1.1 J/(kg K) at 5 T] [68], Fe_3GaTe_2 [1.67 J/(kg K) at 5 T] [69], CrI_3 [4.24 J/(kg K) at 5 T] [70], $MnBi_2Te_4$ [2.48 J/(kg K) at 6 T] [71], $CrCl_3$ [14.6 J/(kg K) at 5 T] [72]. For $H \parallel a$ and $H \parallel c$, the $-\Delta S_M^{max}$ reaches 5.09 and 4.74 J/(kg K) at 5 T, respectively. Heat-capacity measurements under $H \parallel c$ were further performed to provide an additional thermodynamic examination, as shown in Fig. S9 (Note S8 in SM [27]). The heat-capacity-derived entropy change and ΔT_{ad} exhibit a pronounced field-dependent response near the magnetic transition, supporting the magnetocaloric behavior inferred from the magnetization measurements [73,74]. In order to analyze the anisotropy of magnetocaloric effect, the rotating magnetic entropy change $-\Delta S_M^R$ induced by rotating the applied magnetic field from the easily magnetized *b* axis to the *a* or *c* axis direction can be represented as

$$-\Delta S_M^R(b \to a) = \Delta S_M(a) - \Delta S_M(b) \quad (5)$$

$$-\Delta S_M^R(b \to c) = \Delta S_M(c) - \Delta S_M(b) \quad (6)$$

based on Eqs. (5) and (6), the calculated $-\Delta S_M^R$ within the temperature range from 84 to 204 K at 5 T is depicted in

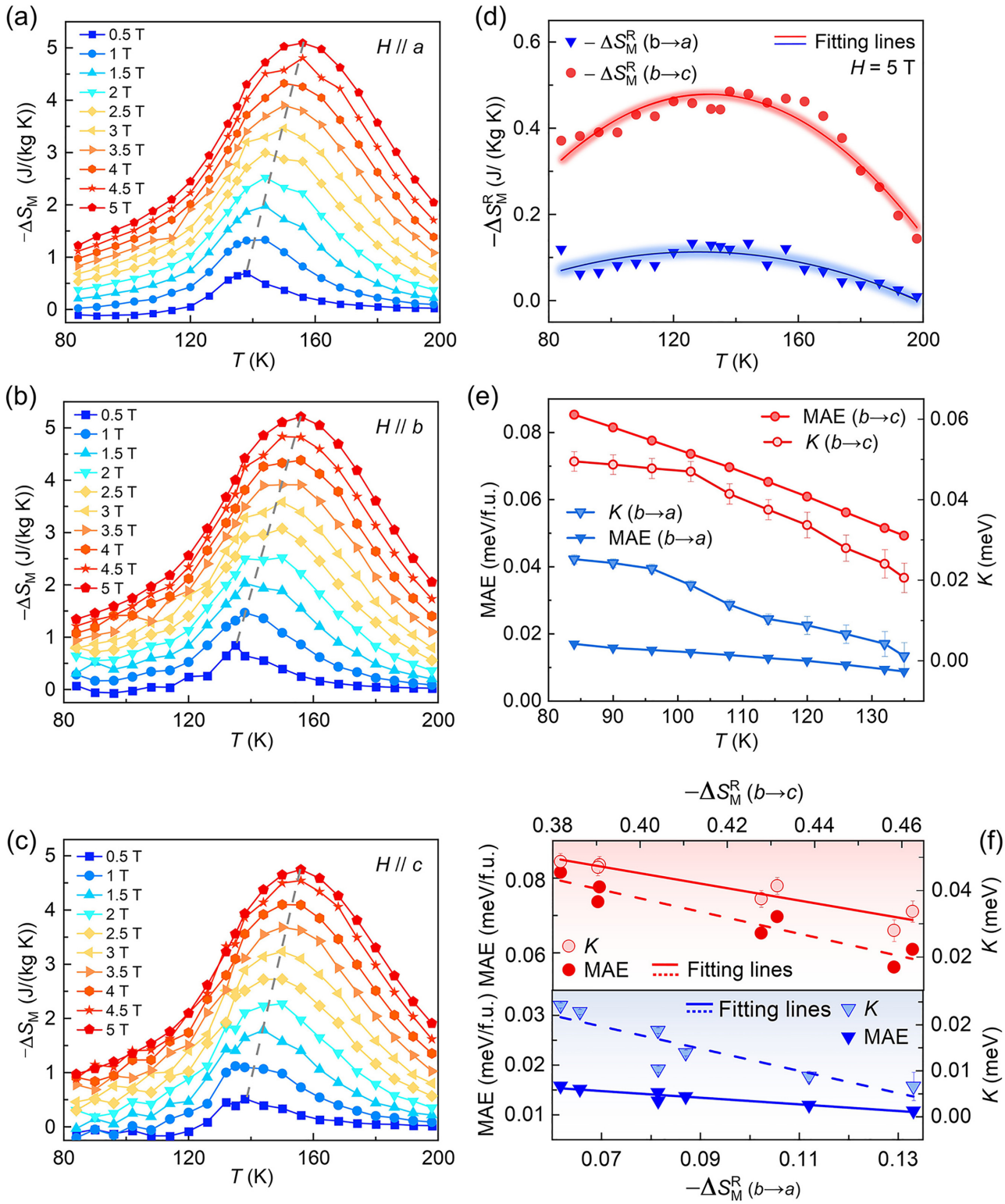

FIG. 3. Temperature dependence of $-\Delta S_M$ under different fields with (a) $H \parallel a$, (b) $H \parallel b$, and (c) $H \parallel c$. (d) Temperature dependence of magnetic entropy change $-\Delta S_M^R$ obtained by rotating from the b axis to the $a$and the b axes to the c axis in a 5 T field. (e) Temperature dependence of MAE and K along the b axis relative to the c axis and along the b axis relative to the a axis. (f) Variation curves of K and MAE vs rotational magnetic entropy change induced by rotating the external magnetic field from the easily magnetized b axis towards the a-axis or c-axis directions.

Fig. 3(d). The distinct trends of these differential curves are evident: $-\Delta S_M^R(b \to a)$ remains relatively small, with a magnitude of approximately 0.1 J/(kg K), whereas $-\Delta S_M^R(b \to c)$ exhibits a significantly larger disparity, reaching a maximum difference of ~0.4 J/(kg K). This latter value far exceeds the rotational magnetic entropy reported

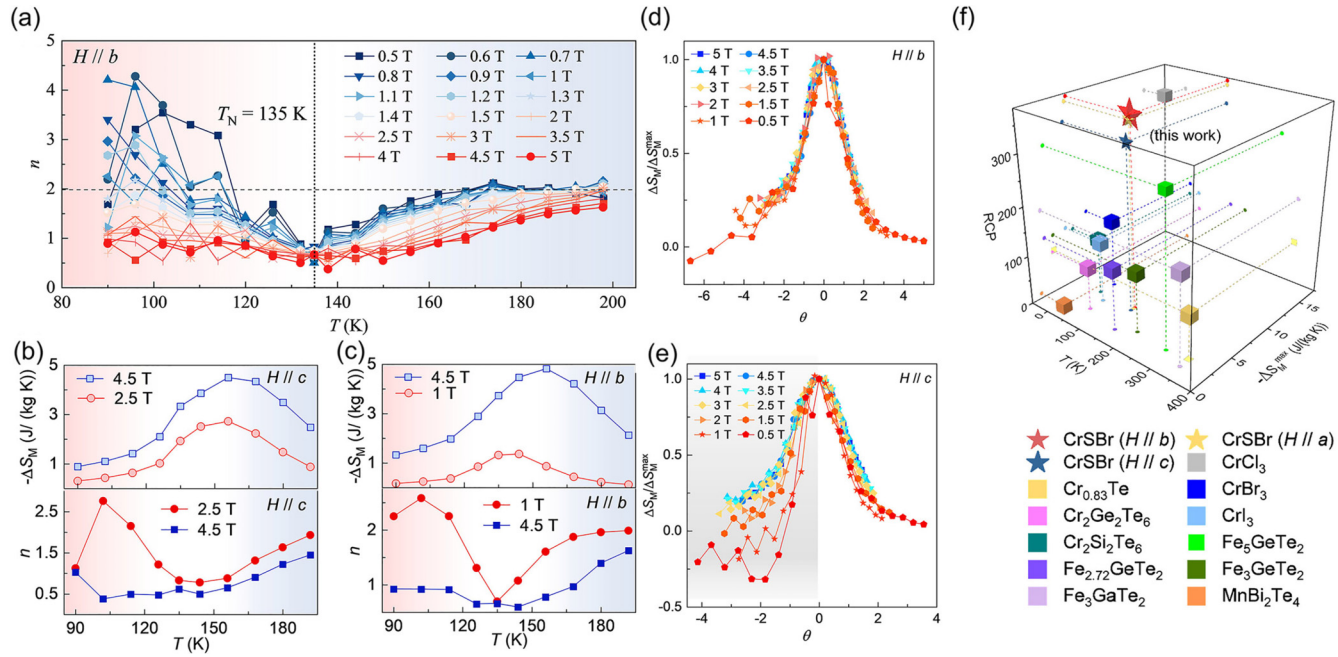

FIG. 4. The temperature dependence of n(T) in various fields with (a) $H \parallel b$. $-\Delta S_{\rm M}(T)$ and the corresponding exponent n at magnetic fields of 1 and 4.5 T with (b) $H \parallel b$. $-\Delta S_{\rm M}(T)$ and the corresponding exponent n at magnetic fields of 2.5 and 4.5 T with (c) $H \parallel c$. Normalized $\Delta S_{\rm M}/\Delta S_{\rm M}^{\rm max}$ for (d) $H \parallel b$ and (e) $H \parallel c$ as a function of the rescaled temperature θ. (f) Comparative summary of the $-\Delta S_{\rm M}^{\rm max}$, transition temperature, and the *RCP* values for representative vdW magnetic materials under comparable magnetic-field conditions [18,24,68–72,76–80].

for $Fe_{2.72}GeTe_2$ [75], underscoring strong triaxial magnetic anisotropy inherent to this lattice-anisotropy system. Such pronounced directional contrast highlights the dominant role of crystallographic orientation in governing spin-lattice interactions and entropy redistribution.

To precisely characterize magnetic anisotropy, in addition to previously calculated K, the MAE is also available, which can be estimated by calculating the area between the magnetization curves obtained when a magnetic field is applied along the easy axis and the hard plane as

$$\text{MAE} = \int_0^{H_{\rm ext}} \{M(H//\text{easy-axis}) - M(H//\text{hard-axis})\} dH, \tag{7}$$

where the integration area is considered as the energy cost for magnetization in a certain direction other than the preferred axis and performed from 0 T to the field at which saturation magnetization is achieved, typically at 5 T. Figure 3(e) shows the temperature-dependent MAE and K from b to c axis and b to a axis. With increasing temperature below $T_{\rm N}$, the MAE and K decrease nearly linearly. The MAE and K between the b to c axis are much higher than those for the b to a axis, highlighting the material's inherent triaxial anisotropy. Figure 3(f) depicts temperature-dependent MAE and K as a function of $-\Delta S_{\rm M}^{\rm R}$. Intuitively, for both the $b \to a$ and $b \to c$ axes, the MAE and K exhibit a negative linear relationship with $-\Delta S_{\rm M}^{\rm R}$ as temperature increases, which indicates a strong relationship between $-\Delta S_{\rm M}^{\rm R}$ and the MAE. Based on Eqs. (5)–(7), the correlation can be established between $-\Delta S_{\rm M}^{\rm R}$ and the MAE as follows:

$$\begin{aligned} -\Delta S_{\rm M}^{\rm R}(H_{\rm ext}, T) &= \Delta S_{\rm M}(H_{\rm ext}// \text{ hard}, T) - \Delta S_{\rm M}(H_{\rm ext}// \text{ easy}, T) \\ &= \int_0^{H_{\rm ext}} \left\{ \frac{\partial M(H//\text{easy}, T)}{\partial T} - \frac{\partial M(H//\text{hard}, T)}{\partial T} \right\} dH \\ &= \frac{\partial E_{\rm MAE}}{\partial T}, \end{aligned} \tag{8}$$

clearly from Eq. (8), the magnetic entropy anisotropy is related to the derivative of the MAE, which is supported by our experimental results as shown in Fig. 3(f). In fact, it is understandable that the MAE reduction at a finite temperature is related to the anisotropic entropy because the MAE is the difference in free energy, which includes the internal energy and entropy terms. Thus the magnetic anisotropy can lead to a modification of the magnetization curves to modulate anisotropic magnetocaloric properties.

The $-\Delta S_{\rm M}$ can be used to quantitatively analyze the critical exponent to understand the critical behavior. Around the second-order phase transition, the field dependence of

the maximum magnetic entropy change shows a power law: $-\Delta S_M^{max} = aH^n$, where a is a constant and the exponent n is given by [81–83]:

$$n(T, H) = \frac{d \ln |\Delta S_M|}{d \ln H}. \quad (9)$$

Figure 4(a) shows the temperature dependence of n(T) for $H \parallel b$, including both the full field range from 0.5 to 5 T and the refined low-field data between 0.5 and 1.5 T. The refined low-field dataset provides a clearer view of the field evolution around the saturation/metamagnetic region, while the full-field dataset shows the overall evolution of n(T) up to 5 T. For $T < T_N$, when $H \leqslant H_S$ (near 1 T), the enhancement of n above 2 can be observed, suggesting complex AFM behavior at low fields. Nevertheless, as $H > 1$ T, the value of n drops rapidly to around 1 and remains stable, indicating the field-induced first-order magnetic transitions as inferred from Banerjee's criterion. For $T > T_N$, the value of n tends to 2 as a consequence of the Curie-Weiss law. Similar temperature-dependent n behaviors can be seen for $H \parallel c$ and $H \parallel a$, as shown in Figs. S10(a) and S10(b) in SM [27]. In particular, due to the larger H_S for $H \parallel c$ than that for $H \parallel b$, the value of n exceeding 2 occurs in the high critical field near 2.5 T below T_N [Figs. 4(b) and 4(c)]. Figures 4(d) and 4(e) display the normalized magnetic entropy change $\Delta S_M/\Delta S_M^{max}$ as a function of the reduced temperature θ with $H \parallel b$ and $H \parallel c$, respectively [84,85]. All curves across various magnetic fields coalesce into a uniform curve above T_N, while distinct branches emerge below T_N, which is related to field-induced first-order magnetic transitions in CrSBr. More pronounced branching profiles below T_N for $H \parallel c$ compared to those for $H \parallel b$ are consistent with their n behaviors [Figs. 4(b) and 4(c)], underscoring strong anisotropy between these crystallographic orientations.

Several magnetocaloric parameters can be further derived from the $-\Delta S_M$ curves, including entropy change (*TEC*), refrigerant capacity (*RC*), and relative cooling power (*RCP*), as presented in Note S9 of SM [27]. These parameters show the same anisotropic trend as ΔS_M^{max}, further supporting the anisotropy-controlled magnetocaloric response. As summarized in Fig. 4(f), comprehensive comparisons of transition-temperature related $-\Delta S_M^{max}$ and *RCP* reveal that CrSBr exhibits a competitive magnetocaloric performance among representative vdW magnetic materials. The field dependences of $-\Delta S_M^{max}$ and *RCP* were further analyzed using the conventional magnetocaloric power-law relations, $-\Delta S_M^{max} \propto H^n$ and RCP $\propto H^m$ [84]. As shown in Note S10 of SM [27], the $H \parallel c$ data yield fitted values of $n = 0.861$ and $m = 1.166$. The corresponding value $\delta_{RCP} \approx 5.9888$ is close to the value of $\delta = 5.719(5)$ derived from the critical isothermal line.

IV. CONCLUSION

In summary, high-quality CrSBr single crystals have been successfully fabricated, and systematic investigations have been performed with regard to its structural, magnetic, and related magnetocaloric properties. As grown by the two-step CVT method, CrSBr single crystal shows a second-order AFM phase transition at 135 K without extra magnetic transitions and magnetic defects. It corresponds to an A-type AFM ground state upon cooling, where FM coupling within the *ac* plane is attributed to superexchange interactions mediated by S/Br anions between Cr ions. The critical analysis supports a second-order magnetic transition near 135 K, with exponents indicating crossoverlike behavior between tricritical mean-field-like and 3D Ising-like regimes. Molecular field approximation analysis and first-principles calculations confirm the triaxial magnetic anisotropy [$K(b \to c) > K(b \to a)$] and spin-flip properties ($K > JS^2$) in CrSBr, which is in connection with the magnetocaloric effect as $\Delta S_M^R \propto K$. It demonstrates that anisotropic entropy contribution dominates the temperature-dependent free energy difference during magnetization along noneasy axis directions. $-\Delta S_M^{max}$ are 5.21, 5.09 and 4.74 J/(kg K) for $H \parallel b$, $H \parallel a$, and $H \parallel c$ at 5 T, respectively, corresponding to a larger $-\Delta S_M^R$ ($b \to a$) than $-\Delta S_M^R$ ($b \to c$), revealing a clear anisotropic magnetocaloric response. Overall, unique in-plane uniaxial anisotropy with A-type magnetic ordering in CrSBr offers a new avenue for developing emerging applications, as demonstrated by our study on triaxial magnetic anisotropy correlated with magnetocaloric properties. On a broader scope, exploiting weak vdW interlayer coupling in CrSBr, triaxial magnetic anisotropy and exotic spin states are tunable through strain and intercalation.

ACKNOWLEDGMENTS

This work was supported by the National Natural Science Foundation of China (Grants No. 62474041, No. 12241401, No. 52403294, and No. 52301230), the Natural Science Foundation of Fujian Province (Grants No. 2023J01521 and No. 2025J01657), the Key research and industrialization projects of technological innovation in Fujian Province (Grant No. 2023XQ010), Project of Yuelushan Center for Industrial Innovation (Grant No. 2025YCHI0121), the Postdoctoral Fellowship Program of CPSF (Grant No. GZC 20252233), the China Postdoctoral Science Foundation (Grant No. 2025M783356), and the project PNCB (Grant No. PN223LH010-081) of the Cuban Ministry of Science, Technology, and Environment.

The authors declare that they have no known competing financial interests or personal relationships that could have appeared to influence the work reported in this paper.

DATA AVAILABILITY

There are no publicly available research data or software supporting this manuscript. Requests for further information or data should be sent to the authors.

[1] Z. Wang, T. Zhang, M. Ding, B. Dong, Y. Li, M. Chen, X. Li, J. Huang, H. Wang, X. Zhao, Y. Li, D. Li, C. Jia, L. Sun, H. Guo, Y. Ye, D. Sun, Y. Chen, T. Yang, J. Zhang, S. Ono, Z. Han, and Z. Zhang, Electric-field control of magnetism in a few-layered

van der Waals ferromagnetic semiconductor, Nat. Nanotechnol. **13**, 554 (2018).

[2] B. Huang, G. Clark, D. R. Klein, D. MacNeill, E. Navarro-Moratalla, K. L. Seyler, N. Wilson, M. A. McGuire, D. H. Cobden, D. Xiao, W. Yao, P. Jarillo-Herrero, and X. Xu, Electrical control of 2D magnetism in bilayer CrI_3, Nat. Nanotechnol. **13**, 544 (2018).

[3] N. D. Mermin and H. Wagner, Absence of ferromagnetism or antiferromagnetism in one- or two-dimensional isotropic heisenberg models, Phys. Rev. Lett. **17**, 1133 (1966).

[4] B. Huang, G. Clark, E. Navarro-Moratalla, D. R. Klein, R. Cheng, K. L. Seyler, D. Zhong, E. Schmidgall, M. A. McGuire, D. H. Cobden, W. Yao, D. Xiao, P. Jarillo-Herrero, and X. Xu, Layer-dependent ferromagnetism in a van der Waals crystal down to the monolayer limit, Nature (London) **546**, 270 (2017).

[5] D. R. Klein, D. MacNeill, J. L. Lado, D. Soriano, E. Navarro-Moratalla, K. Watanabe, T. Taniguchi, S. Manni, P. Canfield, J. Fernández-Rossier, and P. Jarillo-Herrero, Probing magnetism in 2D van der Waals crystalline insulators via electron tunneling, Science **360**, 1218 (2018).

[6] D. Guo, X.-Y. Rui, S. Du, Q.-R. Liang, H. Yang, and S.-J. Zheng, Emerging spintronics applications of magnetic van der Waals heterostructures, Rare Met. **44**, 9336 (2025).

[7] S. Zhao, S. Liu, C. Feng, G. Wang, C. Mao, J. Yang, and J. Yang, Sliding-engineered multiple conductive states in van der Waals VSe_2 devices, Appl. Phys. Lett. **127**, 122102 (2025).

[8] M. E. Ziebel, M. L. Feuer, J. Cox, X. Zhu, C. R. Dean, and X. Roy, CrSBr: An air-stable, two-dimensional magnetic semiconductor, Nano Lett. **24**, 4319 (2024).

[9] K. Lee, A. H. Dismukes, E. J. Telford, R. A. Wiscons, J. Wang, X. Xu, C. Nuckolls, C. R. Dean, X. Roy, and X. Zhu, Magnetic order and symmetry in the 2D semiconductor CrSBr, Nano Lett. **21**, 3511 (2021).

[10] F. Pei, J. Yu, J. Zhou, S. Wang, D. Liu, Y. Yuan, L. Xi, F. Jin, X. Kan, C. Wang, L. Wang, W. Yan, Y. Wu, S. Wang, K. Chen, T. Ma, X. Liu, M. Yang, and Q. Li, Surface-sensitive detection of magnetic phase transition in van der Waals magnet CrSBr, Adv. Funct. Mater. **34**, 2309335 (2024).

[11] M. A. Tschudin, D. A. Broadway, P. Siegwolf, C. Schrader, E. J. Telford, B. Gross, J. Cox, A. E. E. Dubois, D. G. Chica, R. Rama-Eiroa, E. J. G. Santos, M. Poggio, M. E. Ziebel, C. R. Dean, X. Roy, and P. Maletinsky, Imaging nanomagnetism and magnetic phase transitions in atomically thin CrSBr, Nat. Commun. **15**, 6005 (2024).

[12] Y. Shao, F. Dirnberger, S. Qiu, S. Acharya, S. Terres, E. J. Telford, D. Pashov, B. S. Y. Kim, F. L. Ruta, D. G. Chica, A. H. Dismukes, M. E. Ziebel, Y. Wang, J. Choe, Y. J. Bae, A. J. Millis, M. I. Katsnelson, K. Mosina, Z. Sofer, R. Huber, X. Zhu, X. Roy, M. van Schilfgaarde, A. Chernikov, and D. N. Basov, Magnetically confined surface and bulk excitons in a layered antiferromagnet, Nat. Mater. **24**, 391 (2025).

[13] B. Yang, B. Bhujel, D. G. Chica, E. J. Telford, X. Roy, F. Ibrahim, M. Chshiev, M. Cosset-Chéneau, and B. J. v. Wees, Electrostatically controlled spin polarization in Graphene-CrSBr magnetic proximity heterostructures, Nat. Commun. **15**, 4459 (2024).

[14] Y. Chen, K. Samanta, N. A. Shahed, H. Zhang, C. Fang, A. Ernst, E. Y. Tsymbal, and S. S. P. Parkin, Twist-assisted all-antiferromagnetic tunnel junction in the atomic limit, Nature (London) **632**, 1045 (2024).

[15] H. B. Tran, H. Momida, Y.-i. Matsushita, K. Shirai, and T. Oguchi, Insight into anisotropic magnetocaloric effect of CrI_3, Acta Mater. **231**, 117851 (2022).

[16] B. Wang, Y. Wu, Y. Bai, P. Shi, G. Zhang, Y. Zhang, and C. Liu, Origin and regulation of triaxial magnetic anisotropy in the ferromagnetic semiconductor CrSBr monolayer, Nanoscale **15**, 13402 (2023).

[17] K. Yang, G. Wang, L. Liu, D. Lu, and H. Wu, Triaxial magnetic anisotropy in the two-dimensional ferromagnetic semiconductor CrSBr, Phys. Rev. B **104**, 144416 (2021).

[18] H. Chen, C. Hu, Z. Xia, L. Jiang, H. Xuan, Y. Fang, B. Qian, J. Yao, and Z. Han, Large relative cooling power arising from consecutive magnetic phase transitions in van der Waals CrSBr, Appl. Phys. Lett. **127**, 252403 (2025).

[19] A. Canetta, S. Volosheniuk, S. Satheesh, J. P. Alvarinhas Batista, A. Castellano, R. Conte, D. G. Chica, K. Watanabe, T. Taniguchi, X. Roy, H. S. J. van der Zant, M. Burghard, M. J. Verstraete, and P. Gehring, Impact of spin-entropy on the thermoelectric properties of a 2D magnet, Nano Lett. **24**, 6513 (2024).

[20] E. J. Telford, A. H. Dismukes, R. L. Dudley, R. A. Wiscons, K. Lee, D. G. Chica, M. E. Ziebel, M.-G. Han, J. Yu, S. Shabani, A. Scheie, K. Watanabe, T. Taniguchi, D. Xiao, Y. Zhu, A. N. Pasupathy, C. Nuckolls, X. Zhu, C. R. Dean, and X. Roy, Coupling between magnetic order and charge transport in a two-dimensional magnetic semiconductor, Nat. Mater. **21**, 754 (2022).

[21] J. Klein, B. Pingault, M. Florian, M.-C. Heißenbüttel, A. Steinhoff, Z. Song, K. Torres, F. Dirnberger, J. B. Curtis, M. Weile, A. Penn, T. Deilmann, R. Dana, R. Bushati, J. Quan, J. Luxa, Z. Sofer, A. Alù, V. M. Menon, U. Wurstbauer, M. Rohlfing, P. Narang, M. Lončar, and F. M. Ross, The bulk van der Waals layered magnet CrSBr is a quasi-1D material, ACS Nano **17**, 5316 (2023).

[22] F. Marques-Moros, C. Boix-Constant, S. Mañas-Valero, J. Canet-Ferrer, and E. Coronado, Interplay between optical emission and magnetism in the van der Waals magnetic semiconductor CrSBr in the two-dimensional limit, ACS Nano **17**, 13224 (2023).

[23] A. Scheie, M. Ziebel, D. G. Chica, Y. J. Bae, X. Wang, A. I. Kolesnikov, X. Zhu, and X. Roy, Spin waves and magnetic exchange Hamiltonian in CrSBr, Adv. Sci. **9**, 2202467 (2022).

[24] Z. Lin, L. Zeng, S. Fan, L. Zhang, Y. Chen, J. Yang, and Z. Huang, Critical behavior and large magnetocaloric properties in a van der Waals ferromagnet $CrBr_3$, Phys. Rev. Appl. **23**, 024027 (2025).

[25] J. Rodríguez-Carvajal, Recent advances in magnetic structure determination by neutron powder diffraction, Physica B **192**, 55 (1993).

[26] Y.-K. Wang, Z.-C. Lin, S.-X. Hu, J.-P. Xu, W. Yin, T. Zhu, P.-Y. Zhang, K.-W. Li, W.-Y. Yang, F.-W. Wang, C.-S. Wang, Z.-C. Luo, and J.-B. Yang, An efficient magnetic modification strategy: Strain-induced ferromagnetic ordering and anomalous thermal expansion of Ce_2Fe_{17}, Rare Met. **44**, 7763 (2025).

[27] See Supplemental Material at http://link.aps.org/supplemental/10.1103/g97j-4cz4 for experimental details, sample characterization, additional direction-dependent magnetic measurements, and supplementary data and analyses of the anisotropic magnetocaloric effect in CrSBr, which includes Refs. [28–45].

[28] A. Arrott, Criterion for ferromagnetism from observations of magnetic isotherms, Phys. Rev. **108**, 1394 (1957).

[29] A. Arrott and J. E. Noakes, Approximate equation of state for nickel near its critical temperature, Phys. Rev. Lett. **19**, 786 (1967).

[30] J. S. Kouvel and M. E. Fisher, Detailed magnetic behavior of nickel near its curie point, Phys. Rev. **136**, A1626 (1964).

[31] M. E. Fisher, The theory of equilibrium critical phenomena, Rep. Prog. Phys. **31**, 418 (1968).

[32] A. K. Pramanik and A. Banerjee, Critical behavior at paramagnetic to ferromagnetic phase transition in $Pr_{0.5}Sr_{0.5}MnO_3$: A bulk magnetization study, Phys. Rev. B **79**, 214426 (2009).

[33] R. B. Griffiths, Proposal for notation at tricritical points, Phys. Rev. B **7**, 545 (1973).

[34] R. B. Griffiths, Thermodynamic functions for fluids and ferromagnets near the critical point, Phys. Rev. **158**, 176 (1967).

[35] B. Widom, Equation of state in the neighborhood of the critical point, J. Chem. Phys. **43**, 3898 (1965).

[36] G. S. Rushbrooke, On the thermodynamics of the critical region for the ising problem, J. Chem. Phys. **39**, 842 (1963).

[37] R. B. Griffiths, Thermodynamic inequality near the critical point for ferromagnets and fluids, Phys. Rev. Lett. **14**, 623 (1965).

[38] B. D. Josephson, Inequality for the specific heat: I. derivation, Proc. Phys. Soc. **92**, 269 (1967).

[39] Y. Liu and C. Petrovic, Critical behavior of quasi-two-dimensional semiconducting ferromagnet $Cr_2Ge_2Te_6$, Phys. Rev. B **96**, 054406 (2017).

[40] C. Boix-Constant, S. Mañas-Valero, A. M. Ruiz, A. Rybakov, K. A. Konieczny, S. Pillet, J. J. Baldoví, and E. Coronado, Probing the spin dimensionality in single-layer CrSBr van der Waals heterostructures by magneto-transport measurements, Adv. Mater. **34**, 2204940 (2022).

[41] B. Widom, Degree of the critical isotherm, J. Chem. Phys. **41**, 1633 (1964).

[42] W. Liu, X. Guo, J. Schwartz, H. Xie, N. U. Dhale, S. H. Sung, A. L. N. Kondusamy, X. Wang, H. Zhao, D. Berman, R. Hovden, L. Zhao, and B. Lv, A three-stage magnetic phase transition revealed in ultrahigh-quality van der Waals bulk magnet CrSBr, ACS Nano **16**, 15917 (2022).

[43] Y. Zhang, Review of the structural, magnetic and magnetocaloric properties in ternary rare earth RE_2T_2X type intermetallic compounds, J. Alloys Compd. **787**, 1173 (2019).

[44] L. Li and M. Yan, Recent progresses in exploring the rare earth based intermetallic compounds for cryogenic magnetic refrigeration, J. Alloys Compd. **823**, 153810 (2020).

[45] Y. Zhang, H. Li, J. Wang, X. Li, Z. Ren, and G. Wilde, Structure and cryogenic magnetic properties in Ho_2BaCuO_5 cuprate, Ceram. Int. **44**, 1991 (2018).

[46] G. Kresse and J. Furthmüller, Efficiency of *ab-initio* total energy calculations for metals and semiconductors using a plane-wave basis set, Comput. Mater. Sci. **6**, 15 (1996).

[47] G. Kresse and J. Furthmüller, Efficient iterative schemes for *ab initio* total-energy calculations using a plane-wave basis set, Phys. Rev. B **54**, 11169 (1996).

[48] J. P. Perdew, K. Burke, and M. Ernzerhof, Generalized gradient approximation made simple, Phys. Rev. Lett. **77**, 3865 (1996).

[49] F. Moro, S. Ke, A. G. del Águila, A. Söll, Z. Sofer, Q. Wu, M. Yue, L. Li, X. Liu, and M. Fanciulli, Revealing 2D magnetism in a bulk CrSBr single crystal by electron spin resonance, Adv. Funct. Mater. **32**, 2207044 (2022).

[50] E. J. Telford, A. H. Dismukes, K. Lee, M. Cheng, A. Wieteska, A. K. Bartholomew, Y.-S. Chen, X. Xu, A. N. Pasupathy, X. Zhu, C. R. Dean, and X. Roy, Layered antiferromagnetism induces large negative magnetoresistance in the van der Waals semiconductor CrSBr, Adv. Mater. **32**, 2003240 (2020).

[51] Y. Wang, N. Luo, J. Zeng, L.-M. Tang, and K.-Q. Chen, Magnetic anisotropy and electric field induced magnetic phase transition in the van der Waals antiferromagnet CrSBr, Phys. Rev. B **108**, 054401 (2023).

[52] P. W. Anderson, Antiferromagnetism. Theory of superexchange interaction, Phys. Rev. **79**, 350 (1950).

[53] F. Long, K. Mosina, R. Hübner, Z. Sofer, J. Klein, S. Prucnal, M. Helm, F. Dirnberger, and S. Zhou, Intrinsic magnetic properties of the layered antiferromagnet CrSBr, Appl. Phys. Lett. **123**, 222401 (2023).

[54] J. L. Lado and J. Fernández-Rossier, On the origin of magnetic anisotropy in two dimensional CrI_3, 2D Mater. **4**, 035002 (2017).

[55] Y. Peng, Z. Lin, G. Tian, J. Yang, P. Zhang, F. Wang, P. Gu, X. Liu, C.-W. Wang, M. Avdeev, F. Liu, D. Zhou, R. Han, P. Shen, W. Yang, S. Liu, Y. Ye, and J. Yang, Controlling spin orientation and metamagnetic transitions in anisotropic van der Waals antiferromagnet $CrPS_4$ by hydrostatic pressure, Adv. Funct. Mater. **32**, 2106592 (2022).

[56] Y. Zhang, K. Deng, X. Zhang, M. Wang, Y. Wang, C. Liu, J.-W. Mei, S. Kumar, E. F. Schwier, K. Shimada, C. Chen, and B. Shen, In-plane antiferromagnetic moments and magnetic polaron in the axion topological insulator candidate $EuInAs_2$, Phys. Rev. B **101**, 205126 (2020).

[57] Z. Lin, Y. Peng, B. Wu, C. Wang, Z. Luo, and J. Yang, Magnetic van der Waals materials: Synthesis, structure, magnetism, and their potential applications, Chin. Phys. B **31**, 087506 (2022).

[58] L. J. de Jongh, Experiments on simple magnetic model systems, J. Appl. Phys. **49**, 1305 (1978).

[59] T. M. J. Cham, S. Karimeddiny, A. H. Dismukes, X. Roy, D. C. Ralph, and Y. K. Luo, Anisotropic gigahertz antiferromagnetic resonances of the easy axis van der Waals antiferromagnet CrSBr, Nano Lett. **22**, 6716 (2022).

[60] J. Y. Seo, S. Lim, H. J. Shin, K. W. Jeong, J. M. Hong, K. Moon, M. K. Kim, N. Lee, and Y. J. Choi, Probing the weak limit of magnetocrystalline anisotropy through a spin-flop transition in the van der Waals antiferromagnet $CrPS_4$, NPG Asia Mater. **16**, 39 (2024).

[61] S. Li, T. Liu, C. Liu, Y. Wang, H.-Z. Lu, and X. C. Xie, Progress on the antiferromagnetic topological insulator $MnBi_2Te_4$, Natl. Sci. Rev. **11**, nwac296 (2023).

[62] B. K. Banerjee, On a generalised approach to first and second order magnetic transitions, Phys. Lett. **12**, 16 (1964).

[63] S. N. Kaul, Static critical phenomena in ferromagnets with quenched disorder, J. Magn. Magn. Mater. **53**, 5 (1985).

[64] J. C. Le Guillou and J. Zinn-Justin, Critical exponents from field theory, Phys. Rev. B **21**, 3976 (1980).

[65] Y. Gong, X.-F. Miao, T. Samanta, C. Taake, J. Liu, F.-J. Qian, Y.-Y. Shao, Y.-J. Zhang, Q.-Y. Ren, L. Caron, and F. Xu, Anomalous thermal expansion and enhanced magnetocaloric effect in $< 001 >$-textured $Mn_xFe_{5-x}Si_3$ alloys, Rare Met. **43**, 2263 (2024).

[66] X.-J. Xing, Z.-Y. Huo, N. Jiang, X.-L. Wang, Q.-C. Yan, and S.-F. Zhao, High-entropy approach to engineering the magnetoelectric and magnetocaloric properties of manganites, Rare Met. **44**, 2644 (2025).

[67] J. S. Amaral, P. B. Tavares, M. S. Reis, J. P. Araújo, T. M. Mendonça, V. S. Amaral, and J. M. Vieira, The effect of chemical distribution on the magnetocaloric effect: A case study in second-order phase transition manganites, J. NonCryst. Solids **354**, 5301 (2008).

[68] Y. Liu, J. Li, J. Tao, Y. Zhu, and C. Petrovic, Anisotropic magnetocaloric effect in $Fe_{3-x}GeTe_2$, Sci. Rep. **9**, 13233 (2019).

[69] C. Hu, F. Tang, L. Jiang, Y. Chen, H. Chen, Z. Xia, Y. Fang, H. Xuan, B. Qian, and Z. Han, Anisotropic magnetic entropy change and magnetic critical behavior in van der Waals Fe_3GaTe_2, Phys. B Condens. Matter **696**, 416615 (2025).

[70] Y. Liu and C. Petrovic, Anisotropic magnetocaloric effect in single crystals of CrI_3, Phys. Rev. B **97**, 174418 (2018).

[71] Q. Bai and M. Xu, Investigation of field-controlled magnetocaloric switching effect in single crystal antiferromagnetic $MnBi_2Te_4$, Inorg. Chem. Commun. **174**, 114101 (2025).

[72] Q. H. Wang, A. Bedoya-Pinto, M. Blei, A. H. Dismukes, A. Hamo, S. Jenkins, M. Koperski, Y. Liu, Q.-C. Sun, E. J. Telford, H. H. Kim, M. Augustin, U. Vool, J.-X. Yin, L. H. Li, A. Falin, C. R. Dean, F. Casanova, R. F. L. Evans, M. Chshiev, *et al.*, The magnetic genome of two-dimensional van der waals materials, ACS Nano **16**, 6960 (2022).

[73] M. Foldeaki, W. Schnelle, E. Gmelin, P. Benard, B. Koszegi, A. Giguere, R. Chahine, and T. K. Bose, Comparison of magnetocaloric properties from magnetic and thermal measurements, J. Appl. Phys. **82**, 309 (1997).

[74] G. V. Brown, Magnetic heat pumping near room temperature, J. Appl. Phys. **47**, 3673 (1976).

[75] W. Liu, Y. Wang, J. Fan, L. Pi, M. Ge, L. Zhang, and Y. Zhang, Field-dependent anisotropic magnetic coupling in layered ferromagnetic $Fe_{3-x}GeTe_2$, Phys. Rev. B **100**, 104403 (2019).

[76] X. Feng, J. Li, and J. Wu, Anisotropy of magnetocaloric effect in Fe_3GeTe_2, Phys. B Condens. Matter **625**, 413478 (2022).

[77] R. Liang, J. Liu, L. Zhou, and N. Tang, Large relative cooling power in van der Waals room-temperature ferromagnet Fe_5GeTe_2, Appl. Phys. Lett. **124**, 182406 (2024).

[78] S. Purwar, S. Changdar, S. Ghosh, T. K. Bhowmik, and S. Thirupathaiah, Intricate magnetic interactions and topological Hall effect observed in itinerant room-temperature layered ferromagnet $Cr_{0.83}Te$, Acta Mater. **271**, 119898 (2024).

[79] Y. Sun and X. Luo, Magnetic entropy scaling in ferromagnetic semiconductor $CrGeTe_3$, Phys. Status Solidi (b) **256**, 1900052 (2019).

[80] Y. Liu and C. Petrovic, Anisotropic magnetic entropy change in $Cr_2X_2Te_6$ (X = Si and Ge), Phys. Rev. Mater. **3**, 014001 (2019).

[81] D. Guo, L. M. Moreno-Ramírez, C. Romero-Muñiz, Y. Zhang, J.-Y. Law, V. Franco, J. Wang, and Z. Ren, First- and second-order phase transitions in RE_6Co_2Ga (RE = Ho, Dy or Gd) cryogenic magnetocaloric materials, Sci. China Mater. **64**, 2846 (2021).

[82] J. Y. Law, V. Franco, L. M. Moreno-Ramírez, A. Conde, D. Y. Karpenkov, I. Radulov, K. P. Skokov, and O. Gutfleisch, A quantitative criterion for determining the order of magnetic phase transitions using the magnetocaloric effect, Nat. Commun. **9**, 2680 (2018).

[83] L. M. Moreno-Ramírez, J. Y. Law, S. S. Pramana, A. K. Giri, and V. Franco, Analysis of the magnetic field dependence of the isothermal entropy change of inverse magnetocaloric materials, Results Phys. **22**, 103933 (2021).

[84] V. Franco and A. Conde, Scaling laws for the magnetocaloric effect in second order phase transitions: From physics to applications for the characterization of materials, Int. J. Refrig. **33**, 465 (2010).

[85] V. Franco, A. Conde, J. M. Romero-Enrique, and J. S. Blázquez, A universal curve for the magnetocaloric effect: An analysis based on scaling relations, J. Phys.: Condens. Matter **20**, 285207 (2008).